nature nanotechnology

Letter

https://doi.org/10.1038/s41565-022-01309-8

Evidence of frustrated magnetic interactions in a Wigner–Mott insulator

Received: 1 May 2022

Accepted: 28 November 2022

Published online: 16 January 2023

Check for updates

Yanhao Tang[1,2], Kaixiang Su[3], Lizhong Li[1], Yang Xu[1], Song Liu[4], Kenji Watanabe[5], Takashi Taniguchi[5], James Hone[4], Chao-Ming Jian[6], Cenke Xu[3], Kin Fai Mak[1,6,7] ✉ & Jie Shan[1,6,7] ✉

Electrons in two-dimensional semiconductor moiré materials are more delocalized around the lattice sites than those in conventional solids[1,2]. The non-local contributions to the magnetic interactions can therefore be as important as the Anderson superexchange[3], which makes the materials a unique platform to study the effects of competing magnetic interactions[3,4]. Here we report evidence of strongly frustrated magnetic interactions in a Wigner–Mott insulator at a two-thirds (2/3) filling of the moiré lattice in angle-aligned WSe_2/WS_2 bilayers. Magneto-optical measurements show that the net exchange interaction is antiferromagnetic for filling factors below 1 with a strong suppression at a 2/3 filling. The suppression is lifted on screening of the long-range Coulomb interactions and melting of the Wigner–Mott insulators by a nearby metallic gate. The results can be qualitatively captured by a honeycomb-lattice spin model with an antiferromagnetic nearest-neighbour coupling and a ferromagnetic second-neighbour coupling. Our study establishes semiconductor moiré materials as a model system for lattice-spin physics and frustrated magnetism[5].

Moiré structures formed by semiconducting transition metal dichalcogenides (TMDs) provide a physical realization of the extended Hubbard models[1,6–19]. Correlated insulating states, which include both Mott insulators[6–9,17,18] and Wigner–Mott insulators[6,7,15,20], were recently observed in the strong correlation limit. The ground states and low-energy excited states of these correlated insulators are defined by the magnetic exchange interactions between localized spins[1,10,12,21,22]. Compared with real solids, electrons in the moiré lattice experience much weaker periodic potentials that are well approximated by harmonic potentials, and the Wannier functions extend over an appreciable portion of a unit cell[1,2,10,13]. This makes the non-local contributions to the exchange interactions, which are usually negligible in atomic-scale Hubbard systems, relevant. Recent theoretical studies show that a ferromagnetic (FM) direct-exchange contribution (that is, proportional to the interaction) can be tuned to compete with an antiferromagnetic (AF) superexchange contribution (that is, inversely proportional to the interaction) to induce a rich phase diagram[3,4,23]. However, the impact of non-local interactions on the moiré spin physics needs to be examined experimentally.

We focused on the Wigner–Mott insulator state at a two-thirds (2/3) filling of the moiré lattice to reveal the frustrated magnetic interactions in angle-aligned WSe_2/WS_2 bilayers by magneto-optical measurements (Fig. 1). The bilayers formed a triangular moiré lattice with a period of about 8 nm (refs. 6, 7, 24) and a type II band alignment (Fig. 1b). The physics of the topmost moiré valence band can be mapped to a single-band triangular-lattice Hubbard model with a

[1]School of Applied and Engineering Physics, Cornell University, Ithaca, NY, USA. [2]Interdisciplinary Center for Quantum Information, Zhejiang Province Key Laboratory of Quantum Technology, and Department of Physics, Zhejiang University, Hangzhou, China. [3]Department of Physics, University of California, Santa Barbara, CA, USA. [4]Department of Mechanical Engineering, Columbia University, New York, NY, USA. [5]National Institute for Materials Science, Tsukuba, Japan. [6]Laboratory of Atomic and Solid State Physics, Cornell University, Ithaca, NY, USA. [7]Kavli Institute at Cornell for Nanoscale Science, Ithaca, NY, USA. ✉e-mail: kinfai.mak@cornell.edu; jie.shan@cornell.edu

https://doi.org/10.1038/s41565-022-01309-8

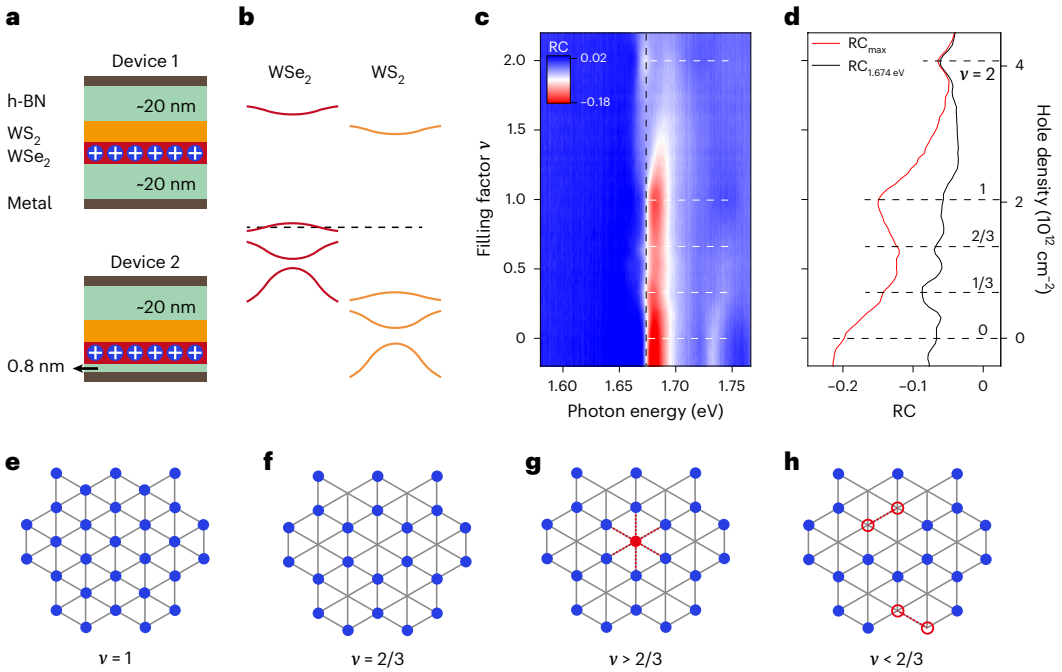

Fig. 1 | Correlated insulating states in WSe_2/WS_2 moiré lattices. a, Cross-sectional schematics of the two types of devices investigated in this study. The WSe_2/WS_2 moiré lattice is hole-doped with holes (positive charges) that reside in the WSe_2 layer. The bottom gate electrode is about 20 nm and 1 nm below the WSe_2 layer in devices 1 and 2, respectively. **b**, Schematic moiré band structure. The Fermi level (dashed line) is inside the first moiré valence band of WSe_2. **c**, RC spectrum of device 1 at 1.7 K as a function of filling factor (left) and doping density (right). RC enhancement near the fundamental moiré exciton resonance of WSe_2 is observed at several commensurate filling factors (dashed horizontal lines). **d**, A linecut in **c** at 1.674 eV (black line) and the maximum RC of the exciton feature as a function of doping (red line). **e**–**h**, Charge configurations at zero temperature on the underlying triangular moiré lattice for $\nu = 1$ (**e**), 2/3 (**f**), slightly above 2/3 (**g**) and below 2/3 (**h**). Filled circles denote occupied sites. In **g**, an extra hole resides at the centre site of a honeycomb formed by the occupied sites; in **h**, the doped vacancies (empty circles) are assumed to reside on a pair of nearest-neighbour sites in a spin model to account for χ near $\nu = 2/3$.

locked spin-valley pseudospin[1] (referred to simply as spin below). The size of the electron Wannier function was about 2 nm (refs. 1, 10). The system was in the strong correlation limit with a nearest-neighbour hopping constant ($t \approx 1$–2 meV) much smaller than both the on-site ($U \approx 100$–200 meV) and the nearest-neighbour Coulomb repulsion ($V \approx 50$ meV) (refs. 1, 6).

We studied two types of devices with a top and bottom gate (Fig. 1a). In both types, the gates were made of either graphite or $TaSe_2$ (a TMD metal) electrodes and hexagonal boron nitride (h-BN) dielectrics. The gates could continuously tune the hole density in the moiré bilayer; a filling factor $\nu = 1$ denotes one hole per moiré site or a half-filled moiré valence band. In device 1, both gate electrodes were about 20 nm away from the moiré bilayer and had a negligible screening effect. In device 2, the bottom gate electrode ($TaSe_2$) was placed about 1 nm below the moiré bilayer, which practically screened out all but the on-site Coulomb repulsion in the moiré lattice. We identified the magnetic response associated with the Wigner–Mott insulators by contrasting the behaviour of the two types of devices. Details on the device fabrication and measurements are provided in Methods.

Figure 1c shows the density-dependent reflectance contrast (RC) spectrum of device 1 near the fundamental moiré exciton resonance[25,26] of WSe_2 at a temperature of $T = 1.7$ K. The moiré density was about 2.0×10^{12} cm^{-2}. Enhancements in the exciton spectral weight were identified at $\nu = 1$, 2/3 and 1/3 (Fig. 1d). The enhancements arose from the formation of a Mott or charge-transfer insulator[10] at $\nu = 1$ (Fig. 1e) and Wigner–Mott insulators (or generalized Wigner crystals[7]) at $\nu = 2/3$ (Fig. 1f) and 1/3. The latter is a manifestation of the strong long-range V, whereas the Mott state is induced by the strong on-site U. From temperature dependence studies, the two Wigner–Mott insulators melt at around 35 K. These results are consistent with those of previous reports[6,7,15].

We examined the magnetic response of the moiré bilayers by performing magnetic circular dichroism (MCD) measurements near the fundamental moiré exciton resonance of WSe_2 under an out-of-plane magnetic field (Fig. 2). The MCD is the difference between the reflection of left and right circularly polarized incident light normalized by the total reflection. It provides a measure of the magnetization, M, of the moiré bilayer because of the valley-dependent optical selection rules and spin-valley locking in monolayer TMDs[6,27,28]. The magnetic-field-dependent MCD spectrum in Fig. 2a is from device 1 at $\nu = 2/3$ and $T = 1.7$ K. (Extended Data Fig. 1 shows the raw helicity-resolved RC spectra.) The signal is enhanced near the moiré exciton resonance (~1.67 eV). We used the integrated MCD over a narrow spectral window around the resonance to represent M, as described in earlier studies[6,17]. The results were insensitive to the exact choice of the spectral window (Extended Data Fig. 2).

Figure 2b shows the magnetic-field dependence of the integrated MCD of $\nu = 2/3$ at representative temperatures. The MCD increased linearly with magnetic field B for small fields and saturated at around 1 T at 1.7 K. With increasing temperature, the MCD decreased and no clear saturation was observed within the field range of 2 T at high temperatures. We extracted the magnetic susceptibility, $\chi \equiv \lim_{B\to 0} \frac{M}{B}$, from the MCD slope at zero field. Its temperature dependence is summarized in Fig. 2d. The susceptibility follows the Curie–Weiss (CW) law (solid line), $\frac{1}{\chi} = \frac{T-\theta}{C}$, where the Curie constant C is proportional to the saturation magnetization and θ (about −1.4 K) is the CW temperature. The CW law is known to describe the high-temperature magnetic response of interacting local moments with θ reflecting the net exchange interaction energy J between the local moments[29,30] (we adopted the convention of expressing J in kelvin). A negative θ corresponds to an AF exchange interaction. We limited the CW analysis to

https://doi.org/10.1038/s41565-022-01309-8

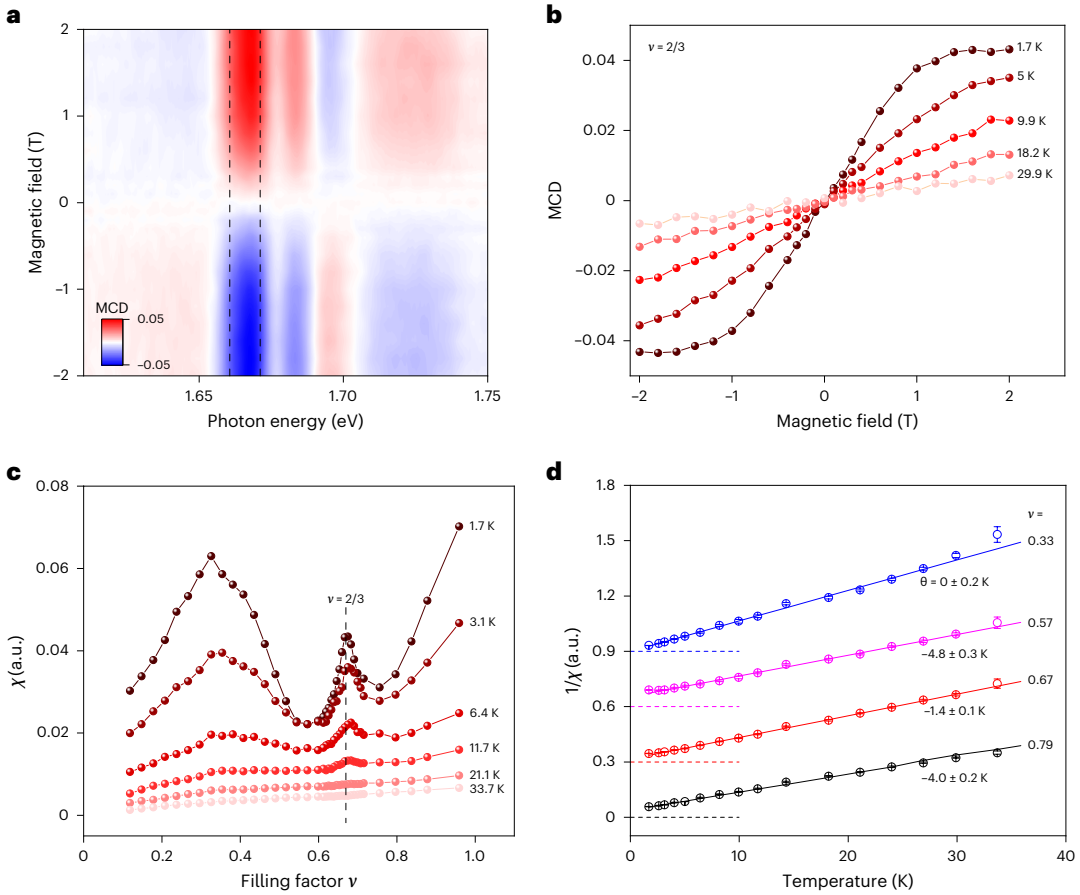

Fig. 2 | Magneto-optical measurements (device 1). a, MCD spectrum as a function of magnetic field at $\nu = 2/3$ and $T = 1.7$ K. The spectrum is integrated over a narrow window around the fundamental moiré exciton resonance (within the two vertical lines) to represent the sample magnetization. **b**, Magnetic-field dependence of integrated MCD at representative temperatures. The MCD saturates above ~1 T at 1.7 K. The slope at zero magnetic field is extracted to represent χ. **c**, Filling dependence of χ at varying temperatures. A sharp peak emerges at 2/3 filling as the temperature decreases. **d**, CW analysis of the temperature dependence of the inverse susceptibility (symbols). The error bars are one-sigma uncertainties of the zero-field slope in **b**. CW temperatures that correspond to the best fits (solid lines) are included. Data for different filling factors are vertically displaced for clarity. The horizontal dashed lines mark where $1/\chi$ is zero. a.u., arbitrary units.

5–35 K (above $|\theta|$ but below the melting temperature of the Wigner–Mott insulator), in which the picture of local moments applies. The fitting results were, however, not sensitive to the precise choice of the temperature range. The picture of local moments is also consistent with Fig. 2b, which reflects the alignment and saturation of the local moments under an external magnetic field. In the low-temperature limit, the saturation field ($B_s \approx 1$ T) also reflected J: a higher Zeeman field was required to overcome a stronger AF exchange to achieve magnetic saturation. At temperatures above J, the magnetic response was strongly affected by thermal excitations.

We performed similar measurements and analysis for the entire filling range of $\nu \leq 1$ (Extended Data Figs. 3 and 4). Figure 2c shows the filling-dependent χ at varying temperatures. At high temperatures, a linear dependence was observed (Extended Data Fig. 5), which reflects the expected linear dependence of the local moment density on filling, $C \propto \nu$. As the temperature decreased below J, χ increased drastically and a non-monotonic filling dependence emerged (Figs. 2c and 3a). Concurrently, both the CW temperature (Fig. 3b) and the saturation field at 1.7 K (Fig. 3c) also exhibited a strongly non-monotonic filling dependence. For all ν values, the CW temperature was negative or close to 0. The three quantities, χ, θ and B_s, were fully consistent with each other. For instance, a small $|\theta|$ was accompanied by a small B_s and a large χ; these are manifestations of a small AF exchange interaction J. The filling dependences for θ and B_s were not exactly identical because of the finite temperature effects for B_s.

The most striking feature of Fig. 3 is the strong suppression of the AF exchange around $\nu = 2/3$. The width of the feature in the filling factor agrees well with the width of the Wigner–Mott insulator at $\nu = 2/3$ (Fig. 1c,d). A similar effect is also likely at around $\nu = 1/3$, but because the local moments were far apart, the exchange energy scale was too small to be fully resolved in this experiment. Suppression of the AF exchange at other fractional fillings between 1/3 and 2/3 was not observed. As the magnetism in the triangular-lattice Hubbard models at generic fillings that involve itinerant carriers is too complex to be resolved in one study, we focused on the most notable observation at fillings around 2/3 below.

To elucidate the role of the Wigner–Mott insulator on the magnetic response at 2/3 filling, we compared the behaviour of devices 1 and 2. In device 2 (Fig. 1a), the bottom gate electrode effectively screened out the long-range Coulomb repulsion and quenched the Wigner–Mott insulator[31]. This is consistent with recent reports[32,33] and is supported by the absence of any enhancement in the exciton RC at $\nu = 2/3$ (Extended Data Fig. 6). Also no longer observable in device 2 were the pronounced peak in χ and the dip in B_s at around 2/3 filling at 1.7 K (Fig. 3a,c). In addition, we were able to perform the CW analysis on the temperature-dependent χ (Extended Data Fig. 7). The presence of a strong correlation probably contributes to the applicability of the CW analysis for interacting local moments here[34,35]. The extracted CW temperature (Fig. 3b) was again negative with a larger magnitude for the entire filling range ($\theta \approx -7$ K at $\nu = 2/3$), which reflects stronger AF

https://doi.org/10.1038/s41565-022-01309-8

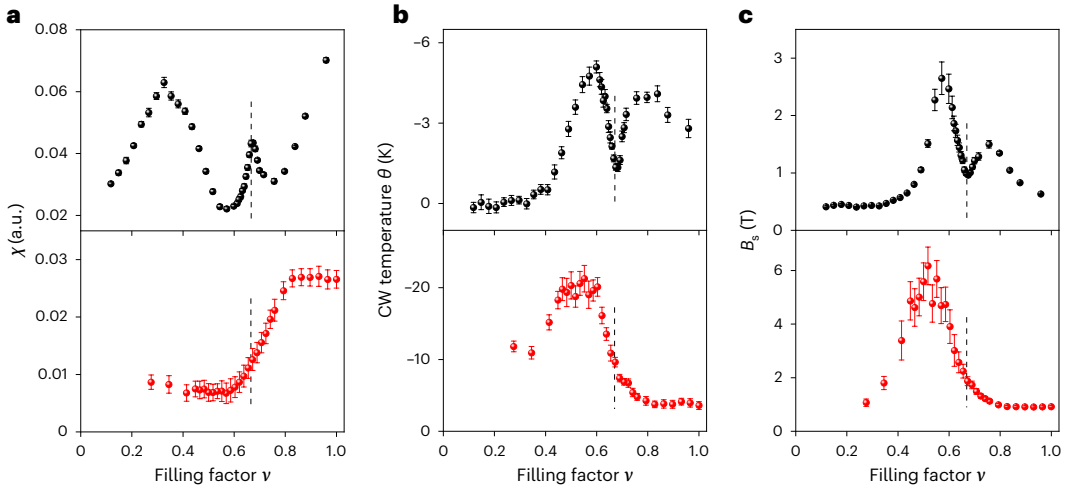

Fig. 3 | Comparison of the magnetic response of devices 1 and 2. a–**c**, Filling dependence of χ at 1.7 K (**a**), the CW temperature (**b**) and the saturation magnetic field at 1.7 K (**c**). Data without gate screening (device 1) and with screening (device 2) are shown in the top and bottom panels, respectively. The strongly suppressed AF exchange at a 2/3 filling (dashed lines) is observed in device 1, but not in device 2. The error bars are one-sigma uncertainties of the zero-field MCD slope (**a**), the CW analysis (**b**) and the Brillouin-function fit as described in Methods (**c**).

interactions between the local moments. The dip in the filling dependence of $|\theta|$ at around $\nu = 2/3$ was no longer observable. All these results indicate that the suppressed AF exchange interaction at a 2/3 filling in device 1 is associated with the Wigner–Mott insulator.

We considered the exchange mechanisms between local moments. The Anderson superexchange, which involves virtual hopping of particles between two neighbouring sites, was AF. When the long-range interactions were negligible, the superexchange was inversely proportional to the on-site U ($\sim \frac{t^2}{U}$). This mechanism contributed to the observed net AF exchange and its enhancement on screening of the Coulomb repulsions. However, the superexchange mechanism alone cannot explain the observed suppression of the net AF exchange near 2/3 filling (Fig. 3b). Other contributions, such as the interaction-assisted hopping and direct exchange, have to be considered[3,4]. These non-local contributions to the exchange interaction are relevant in semiconductor moiré materials because of the harmonic trapping potentials and the extended electron Wannier functions[1,2,10,13]. In particular, the direct exchange is FM and proportional to Coulomb interactions[3]; it can be tuned by screening to compete with the AF superexchange to induce frustrated magnetism.

In the Wigner–Mott insulator at $\nu = 2/3$, holes form a crystal with a honeycomb lattice[20] (Fig. 1f). As the system remains insulating when immediately doped away from a 2/3 filling[36], the spin physics near $\nu = 2/3$ can be captured by a (doped) spin model on the honeycomb lattice (Methods). The spin model is a good approximation in the flat band limit, as in angle-aligned WSe_2/WS_2 (refs. 6, 7). For simplicity, we considered a model with both nearest and second neighbour Heisenberg interactions. We did not make assumptions of the sign of the Heisenberg interactions to begin with, but we showed (Methods) that the experimental data favours an AF nearest-neighbour coupling J_1 and a FM second-neighbour coupling J_2 (both J_1 and J_2 are taken to be positive in our convention). A recent microscopic analysis[3] showed that such a regime is possible. The choice of a FM J_2 is consistent with the observed increase in $|\theta|$ when the long-range interaction was screened (Fig. 3b). Exactly at $\nu = 2/3$, there were three nearest neighbours and six second neighbours per hole. The CW temperature, which is a weighted sum of the exchange interactions[29,30], is hence given by $\theta = -(J_1 - 2J_2)$. The exchange is always AF as long as $J_1 > 2J_2$.

For $\nu \gtrsim 2/3$, the extra holes naturally resided at the centre moiré sites of the honeycomb to minimize the Coulomb repulsion (Fig. 1g). They increased the AF nearest-neighbour links, but did not increase the FM second-neighbour links in the dilute limit. This simple picture implies that filling above 2/3 drove the system 'more AF'. For $\nu \lesssim 2/3$, vacancies were introduced into the honeycomb lattice (Fig. 1h). Introducing a vacancy removes twice as many FM links as AF links. This is identical to the original lattice and hence cannot explain the stronger AF exchange observed in the experiment. However, if we further assume that a fraction of the vacancies ($0 < x \leq 1$) reside on a pair of nearest-neighbour sites, to introduce a pair of vacancies removes 12 FM links but only 5 AF links (Fig. 1h), and hence drives the system more AF (detailed calculations in Methods). Note that we did not attempt to prove that vacancies were, indeed, introduced in pairs here, but a recent theoretical study on TMD moiré materials suggested that doping in pairs could cost less Coulomb repulsion energy under the right conditions[11]. Nevertheless, the spin model with only J_1 and J_2 adopted here is probably too simple to account for all the experimental data near $\nu = 2/3$.

In conclusion, we reveal the frustrated magnetic interactions in semiconductor moiré bilayers in a strong interaction limit through a strongly suppressed AF exchange in the Wigner–Mott insulator at $\nu = 2/3$. We did not observe any clear enhancement or suppression of the net exchange interaction at other commensurate fractional fillings between 1/3 and 2/3, for which charge-ordered states have been reported[6,15,16]. In general, the magnetic interaction in an extended Hubbard system at generic fillings is a complicated problem. Future studies are required to better understand the mechanism of magnetic exchange in the presence of charge order, nematicity[16] and itinerant electrons.

Online content

Any methods, additional references, Nature Portfolio reporting summaries, source data, extended data, supplementary information, acknowledgements, peer review information; details of author contributions and competing interests; and statements of data and code availability are available at https://doi.org/10.1038/s41565-022-01309-8.

References

1. Wu, F., Lovorn, T., Tutuc, E. & MacDonald, A. H. Hubbard model physics in transition metal dichalcogenide moiré bands. *Phys. Rev. Lett.* **121**, 026402 (2018).
2. Wu, F., Lovorn, T., Tutuc, E., Martin, I. & MacDonald, A. H. Topological insulators in twisted transition metal dichalcogenide homobilayers. *Phys. Rev. Lett.* **122**, 086402 (2019).

3. Nicolás, M. D. et al. Non-local interactions in moiré Hubbard systems. *Phys. Rev. Lett.* **128**, 217202 (2022).
4. Hu, N. C. & MacDonald, A. H. Competing magnetic states in transition metal dichalcogenide moiré materials. *Phys. Rev. B* **104**, 214403 (2021).
5. Balents, L. Spin liquids in frustrated magnets. *Nature* **464**, 199–208 (2010).
6. Tang, Y. et al. Simulation of Hubbard model physics in WSe_2/WS_2 moiré superlattices. *Nature* **579**, 353–358 (2020).
7. Regan, E. C. et al. Mott and generalized Wigner crystal states in WSe_2/WS_2 moiré superlattices. *Nature* **579**, 359–363 (2020).
8. Shimazaki, Y. et al. Strongly correlated electrons and hybrid excitons in a moiré heterostructure. *Nature* **580**, 472–477 (2020).
9. Wang, L. et al. Correlated electronic phases in twisted bilayer transition metal dichalcogenides. *Nat. Mater.* **19**, 861–866 (2020).
10. Zhang, Y., Yuan, N. F. Q. & Fu, L. Moiré quantum chemistry: charge transfer in transition metal dichalcogenide superlattices. *Phys. Rev. B* **102**, 201115 (2020).
11. Slagle, K. & Fu, L. Charge transfer excitations, pair density waves, and superconductivity in moiré materials. *Phys. Rev. B* **102**, 235423 (2020).
12. Pan, H., Wu, F. & Das Sarma, S. Band topology, Hubbard model, Heisenberg model, and Dzyaloshinskii–Moriya interaction in twisted bilayer WSe_2. *Phys. Rev. Res.* **2**, 033087 (2020).
13. Pan, H., Wu, F. & Das Sarma, S. Quantum phase diagram of a moiré–Hubbard model. *Phys. Rev. B* **102**, 201104 (2020).
14. Kennes, D. M. et al. Moiré heterostructures as a condensed-matter quantum simulator. *Nat. Phys.* **17**, 155–163 (2021).
15. Huang, X. et al. Correlated insulating states at fractional fillings of the WS_2/WSe_2 moiré lattice. *Nat. Phys.* **17**, 715–719 (2021).
16. Jin, C. et al. Stripe phases in WSe_2/WS_2 moiré superlattices. *Nat. Mater.* **20**, 940–944 (2021).
17. Li, T. et al. Continuous Mott transition in semiconductor moiré superlattices. *Nature* **597**, 350–354 (2021).
18. Ghiotto, A. et al. Quantum criticality in twisted transition metal dichalcogenides. *Nature* **597**, 345–349 (2021).
19. Zhang, Y., Liu, T. & Fu, L. Electronic structures, charge transfer, and charge order in twisted transition metal dichalcogenide bilayers. *Phys. Rev. B* **103**, 155142 (2021).
20. Li, H. et al. Imaging two-dimensional generalized Wigner crystals. *Nature* **597**, 650–654 (2021).
21. Margarita D., Yang Z. & Fu, L. Itinerant spin polaron and metallic ferromagnetism in semiconductor moiré superlattices. Preprint at https://arxiv.org/abs/2206.01221 (2022).
22. Lee, K., Sharma, P., Vafek O. & Changlani, H.J. Triangular lattice Hubbard model physics at intermediate temperatures. Preprint at https://arxiv.org/abs/2209.00664 (2022).
23. Morales-Durán, N., Potasz, P. & MacDonald, A.H. Magnetism and quantum melting in moiré-material Wigner crystals. Preprint at https://arxiv.org/abs/2210.15168 (2022).
24. Jin, C. et al. Observation of moiré excitons in WSe_2/WS_2 heterostructure superlattices. *Nature* **567**, 76–80 (2019).
25. Huang, D., Choi, J., Shih, C.-K. & Li, X. Excitons in semiconductor moiré superlattices. *Nat. Nanotechnol.* **17**, 227–238 (2022).
26. Wilson, N. P., Yao, W., Shan, J. & Xu, X. Excitons and emergent quantum phenomena in stacked 2D semiconductors. *Nature* **599**, 383–392 (2021).
27. Mak, K. F., Xiao, D. & Shan, J. Light–valley interactions in 2D semiconductors. *Nat. Photon.* **12**, 451–460 (2018).
28. Xu, X., Yao, W., Xiao, D. & Heinz, T. F. Spin and pseudospins in layered transition metal dichalcogenides. *Nat. Phys.* **10**, 343–350 (2014).
29. Spal/ek, J. et al. Magnetic susceptibility of semimagnetic semiconductors: the high-temperature regime and the role of superexchange. *Phys. Rev. B* **33**, 3407–3418 (1986).
30. Zheng, W., Singh, R. R. P., McKenzie, R. H. & Coldea, R. Temperature dependence of the magnetic susceptibility for triangular-lattice antiferromagnets with spatially anisotropic exchange constants. *Phys. Rev. B* **71**, 134422 (2005).
31. Tang, Y. et al. Dielectric catastrophe at the Wigner–Mott transition in a moiré superlattice. *Nat. Commun.* **13**, 4271 (2022).
32. Gu, J. et al. Dipolar excitonic insulator in a moiré lattice. *Nat. Phys.* **18**, 395–400 (2022).
33. Zhang, Z. et al. Correlated interlayer exciton insulator in heterostructures of monolayer WSe_2 and moiré WS_2/WSe_2. *Nat. Phys.* **18**, 1214–1220 (2022).
34. Foo, M. L. et al. Charge ordering, commensurability, and metallicity in the phase diagram of the layered Na_xCoO_2. *Phys. Rev. Lett.* **92**, 247001 (2004).
35. Merino, J., Powell, B. J. & McKenzie, R. H. Ferromagnetism, paramagnetism, and a Curie–Weiss metal in an electron-doped Hubbard model on a triangular lattice. *Phys. Rev. B* **73**, 235107 (2006).
36. Li, T. et al. Charge-order-enhanced capacitance in semiconductor moiré superlattices. *Nat. Nanotechnol.* **16**, 1068–1072 (2021).

Methods

Sample and device fabrication

Dual-gate devices of angle-aligned WSe_2/WS_2 heterobilayers were fabricated using a dry-transfer method reported in the literature[6]. In short, atomically thin flakes of each constituent were exfoliated from bulk crystals onto SiO_2–Si substrates, and identified by their RC under an optical microscope. The thickness was determined more accurately by atomic force microscopy. A polymer stamp was used to pick up all of the flakes sequentially. The finished stack was released onto SiO_2–Si substrates with prepatterned Au electrodes. Second harmonic generation was employed to determine the crystal axes of the WSe_2 and WS_2 monolayers before stacking[6]. The main text reports results from a 60°-aligned sample. The results were reproduced in a second 60°-aligned sample (Extended Data Fig. 8). Similar results were also observed in a 0°-aligned sample (Extended Data Fig. 8). For the second type of device, an extra few-layer $TaSe_2$ flake was introduced into the device (Fig. 1a). It was separated from the WSe_2/WS_2 heterobilayer by a bilayer h-BN spacer. The $TaSe_2$ flakes were exfoliated inside a nitrogen-filled glove box to avoid sample degradation. We followed the procedure described in Tang et al.[6] to calibrate the doping density and filling factor of the moiré bilayer. Specifically, we measured the h-BN gate dielectric thickness by atomic force microscopy and used the known dielectric constant of h-BN (~3) to calculate the hole doping density using a parallel plate capacitor model.

Magneto-optical measurements

Details of the MCD measurements were reported in Tang et al.[6] and Li et al.[17]. In short, the devices were mounted in a closed-cycle cryostat with a superconducting magnet (attoDRY 2100). The magnetic field was applied perpendicular to the sample plane. White light from a tungsten halogen lamp was collimated and focused onto the devices (with the power less than 1 nW). The reflected light was detected by a liquid nitrogen-cooled charge-coupled device attached to a grating spectrometer. The polarization of the white light was controlled by a combination of a polarizer and a broadband quarter-wave plate. The WSe_2/WS_2 heterobilayers were grounded during the optical measurements. In device 1, both the top and bottom gate voltages were controlled independently by two Keithley source meters. In device 2, the $TaSe_2$ flake was grounded, and only the top gate voltage was applied to tune the filling factor. In contrast to that of Wang et al.[37], the excitation intensity was kept substantially lower to minimize the perturbation on the correlated states. We also analysed the MCD spectrum rather than a single-wavelength MCD signal so that a sign change in the MCD signal as well as a spectral shift in the exciton resonance with doping can be properly accounted for.

The MCD spectrum is defined as $\mathrm{MCD} = \frac{I_+ - I_-}{I_+ + I_-}$, where I_+ and I_- are, respectively, the spectrum of the reflected left- and right-handed incident light from the sample. The integrated MCD signal is computed as $\frac{\int_{\epsilon_1}^{\epsilon_2} \mathrm{d}\epsilon(\mathrm{MCD})}{\int_{\epsilon_1}^{\epsilon_2} \mathrm{d}\epsilon}$, where ε is the photon energy and the limits of integration are given by the dashed lines in Fig. 2a. We focus on the MCD response in this study rather than the exciton Zeeman splitting as in an earlier study[6]. Although the two methods are generally in good agreement with each other, the MCD gives a better signal-to-noise ratio. It directly reflects the optical Hall response and the spin-valley polarization of the system, and is therefore more straightforward to interpret[17]. In particular, the MCD is easier to analyse than the exciton Zeeman splitting in the presence of multiple exciton peaks at $\nu = 2/3$ which partially overlap in energy (Extended Data Fig. 1). We focused on hole doping, for which a strong MCD is observed (Extended Data Fig. 9). To isolate the local moment response, we also subtracted a small, constant slope at high magnetic fields from the magnetic-field-dependent MCD; this slope arises from the bare exciton Zeeman effect, which is nearly temperature independent.

Determination of the saturation magnetic field

We used the Brillouin function, $\frac{M}{M_s} = \tanh(B/B_s)$, to describe the magnetic-field dependence of the integrated MCD signal or the sample magnetization M. Here B denotes the applied magnetic field and M_s and B_s are the saturation magnetization and magnetic field, respectively. An example is shown in Extended Data Fig. 10 for $\nu = 0.96$ and $T = 1.7$ K. The filling dependence of B_s is shown in Fig. 3c.

Spin model

At 2/3 filling, the charges form a Wigner–Mott crystal with the shape of a honeycomb lattice[20], which is 2/3 of the lattice sites of the original triangular moiré lattice (Fig. 1). We considered filling factors of around 2/3. Although in our experiment the moiré lattice was filled with holes for the entire doping range, we refer to fillings slightly below and above 2/3 as 'electron doping' and 'hole doping', respectively. One key observation we made is that, when immediately doped away from a 2/3 filling, the system remained insulating at low temperatures, based on capacitance measurements[36]. This implies that the doped charges in the flat band system are always immobile, probably due to the presence of long-wavelength moiré disorders and/or a strong correlation. The spin physics of the system near a 2/3 filling was therefore captured by a (doped) spin model on the honeycomb lattice with each immobile hole carrying a spin-1/2 degree of freedom. The effect of moiré disorder was not treated explicitly in our model; it only enters in localizing the doped holes/electrons.

The spin model we adopted has AF nearest-neighbour (nn) coupling J_1, and FM next-nearest-neighbour (nnn) coupling J_2 (in our convention, both J_1 and J_2 are taken to be positive). The Hamiltonian of the spin model takes the following form:

$$H = \sum_{\text{nn bonds}} J_1 \vec{S}_i \cdot \vec{S}_j - \sum_{\text{nnn bonds}} J_2 \vec{S}_i \cdot \vec{S}_j + \sum_{\text{sites}} \vec{h} \cdot \vec{S}_i, \quad (1)$$

where $\vec{S}_i$ is the spin on site i and $\vec{h}$ is the external magnetic field. As the main physics we focused on is observed at a finite temperature, we used a high-temperature expansion to analyse this model. Note that the qualitative results of our high-temperature expansion calculation were insensitive to whether the spin was treated as a classical three-component vector or a quantum spin-1/2 variable. The following calculation was performed using the former treatment.

With hole doping away from 2/3 filling, namely, $\nu > 2/3$, there were two main qualitative findings in the experiments: (1) The CW temperature θ remained negative, but its magnitude increased under hole doping (Fig. 3b); this implies that, speaking overall, the system is AF, and it becomes even 'more AF' under hole doping. (2) The spin susceptibility decreased with hole doping at a low temperature (Fig. 3a), but increased with hole doping at a high temperature (Extended Data Fig. 5).

Figure 1g depicts the set-up for hole doping away from 2/3 filling. The extra hole doped to the system naturally resides at the centre moiré sites of the honeycomb. A doped hole increases the nearest-neighbour AF links in the system (labelled as dashed lines in Figure 1g), but does not increase the FM next-nearest-neighbour links. This simple picture implies that hole doping drives the system 'more AF', and increases $|\theta|$. At filling $\nu = 2(1+p)/3$, the high temperature expansion leads to the following result for θ, expanded to the leading order of doping p (>0):

$$\theta = -[(J_1 - 2J_2) + (3J_1 + 2J_2)p] + O(p^2). \quad (2)$$

As long as $J_1 > 2J_2$, θ is always negative, which signifies AF behaviour. Also, $|\theta|$ increases with hole doping p at the leading order expansion of p, which is consistent with the experimental data. The spin susceptibility χ reads:

$$\chi = \frac{n(1+p)}{3(T-\theta)} \sim \frac{n(1+p)}{3T} + \frac{n(-J_1 + 2J_2 - 4J_1 p)}{3T^2} + O(p^2), \quad (3)$$

where n is the number of holes of the honeycomb at $\nu = 2/3$.

As an example, let us choose $J_1 = 2.5J_2 = 2.5\,A$. We then have $\theta \approx -0.5\,A$. One immediately notices that when $T < 10\,A$, χ decreases with doping p, and when $T > 10\,A$, χ increases with p. All these are consistent with the experimental observations.

With electron doping away from 2/3 filling, namely, $\nu < 2/3$, there are also two main qualitative findings in the experiments: (1) The CW temperature θ remains negative, and the magnitude of $|\theta|$ increases under hole doping (Fig. 3b); this implies that the system still becomes 'more AF' under hole doping. (2) The spin susceptibility always decreases with doping within the temperature range in the experiment (Fig. 3a).

Electron doping was modelled as doping vacancies in our spin model. The experimental facts are somewhat counterintuitive, as doping vacancies normally do not increase $|\theta|$. However, in the following we show that with a simple extra assumption of the configurations of doped vacancies, our model can explain the two experimental facts listed above. The set-up for vacancies doping is depicted in Fig. 1h: we assume that the doped vacancies always reside on a pair of nearest-neighbour sites. Although we do not prove here that the vacancies do form pairs, we note that a similar pair-wise doping in TMD moiré materials in the flat band limit was discussed by Slagle and Fu[11] as a way to minimize the Coulomb repulsion energy. At filling $\nu = 2(1-p)/3$, the high temperature expansion calculation gives the following results:

$$\theta = -\left[(J_1 - 2J_2) - \left(\frac{2J_1}{3} - 2J_2\right)p\right] + O(p^2). \quad (4)$$

As long as $3J_2 > J_1 > 2J_2$, θ is always negative, and $|\theta|$ increases with p, again consistent with the experimental data. The reason $|\theta|$ increases with p is that, on the original lattice model, there are twice as many second neighbour links (FM interactions) as nearest-neighbour links (AF interactions). As the vacancies are 'paired up', doping a pair of vacancies removes 12 FM links, but removes only 5 AF links. Hence, doping vacancies can indeed drive the system more AF, and increase $|\theta|$. The spin susceptibility χ is calculated as:

$$\chi = \frac{n(1-p)}{3(T-\theta)} \sim \frac{n(1-p)}{3T} + \frac{n\left[-J_1 + 2J_2 + \left(\frac{5J_1}{3} - 4J_2\right)p\right]}{3T^2} + O(p^2), \quad (5)$$

Again, as an example, let us choose $J_1 = 2.5J_2 = 2.5\,A$. Then we obtain $\theta \approx -0.5\,A$. We found that as long as $T > A/6$, χ always decreases with p, which is consistent with experimental findings.

Data availability

All data that support the findings of this study are available from the corresponding author upon reasonable request. Source data are provided with this paper.

Code availability

All codes to analyse the reflectance spectrum are available from the corresponding author upon reasonable request.

References

37. Wang, X. et al. Light-induced ferromagnetism in moiré superlattices. *Nature* **604**, 468–473 (2022).

Acknowledgements

We thank V. Elser, L. Fu, E.-A. Kim and S. Kivelson for helpful discussions. This study was supported by the National Science Foundation (NSF) under DMR-1807810 (magneto-optical measurements), the Air Force Office of Scientific Research (AFOSR) under award no. FA9550-20-1-0219 (analysis), and the Cornell Center for Materials Research with funding from the NSF MRSEC program under DMR-1719875 (sample fabrication). It made use of the Cornell NanoScale Facility, an NNCI member supported by NSF grant NNCI-2025233. This research is funded in part by the Gordon and Betty Moore Foundation. The growth of WSe_2 crystals was supported by the US Department of Energy (DOE), Office of Science, Basic Energy Sciences (BES), under award no. DE-SC0019481; the growth of the h-BN crystals was supported by the Elemental Strategy Initiative of MEXT, Japan, and CREST (JPMJCR15F3), JST. C.X. acknowledges support from the NSF under DMR-1920434 and the Simons Investigator program. C.-M.J. acknowledges support from the start-up funding from Cornell University. Y.T. acknowledges support from the National Basic Research Program of China (grant nos. 2022YFA1405400 and 2022YFA1402403), the National Natural Science Foundation of China (grant no. 12274365) and the start-up funding from Zhejiang University.

Author contributions

Y.T. performed the optical measurements and the analysis. Y.T. fabricated the devices with assistance from L.L. and Y.X. S.L. and J.H. grew the bulk TMD crystals. K.W. and T.T. grew the bulk h-BN crystals. K.S., C.-M.J. and C.X. conceived and developed the spin model. K.F.M., J.S. and Y.T. designed the scientific objectives and oversaw the project. K.F.M., J.S., Y.T., K.S., C.-M.J. and C.X. co-wrote the manuscript. All the authors discussed the results and commented on the manuscript.

Competing interests

The authors declare no competing interests.

Additional information

Extended data is available for this paper at https://doi.org/10.1038/s41565-022-01309-8.

Supplementary information The online version contains supplementary material available at https://doi.org/10.1038/s41565-022-01309-8.

Correspondence and requests for materials should be addressed to Kin Fai Mak or Jie Shan.

Peer review information *Nature Nanotechnology* thanks Fengcheng Wu, Su-Fei Shi and the other, anonymous, reviewer(s) for their contribution to the peer review of this work.

https://doi.org/10.1038/s41565-022-01309-8

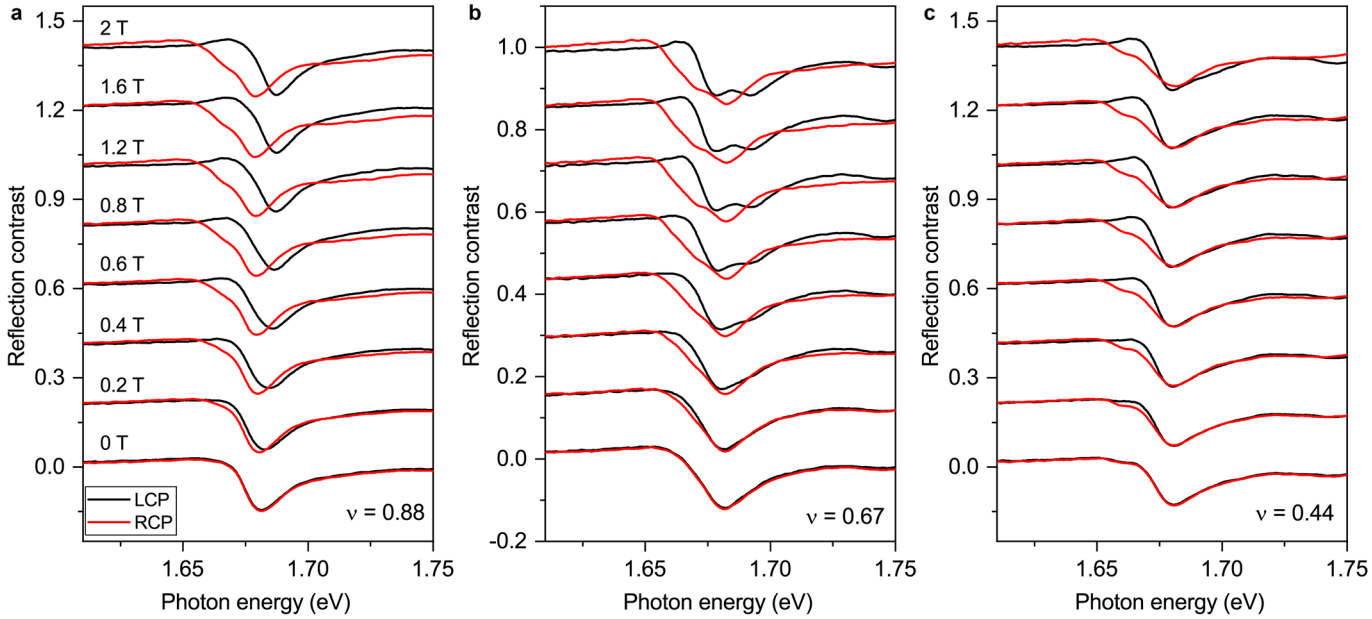

Extended Data Fig. 1 | Helicity-resolved reflectance contrast spectra at varying magnetic fields. a–c, Results for filling factor 0.88 (**a**), 0.67 (**b**) and 0.44 (**c**). The black and red lines denote the left (LCP) and right circularly polarized (RCP) excitations, respectively. The spectra are vertically displaced for clarity.

https://doi.org/10.1038/s41565-022-01309-8

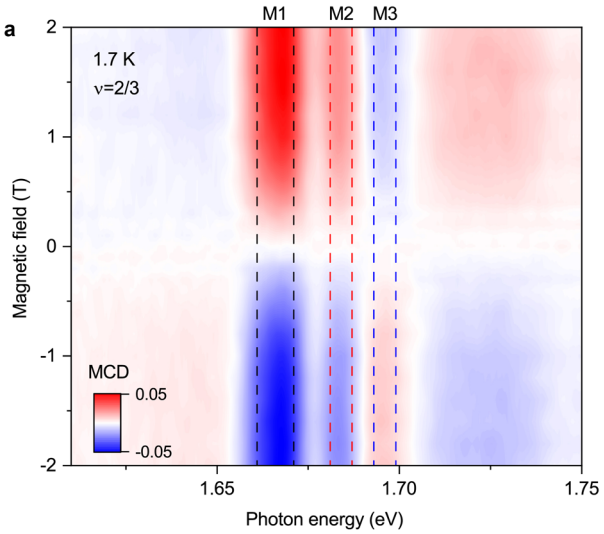

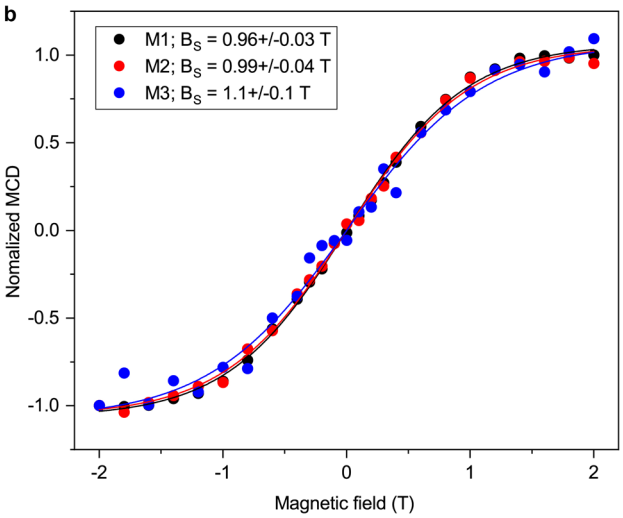

Extended Data Fig. 2 | Analysis of MCD spectra. a, MCD spectrum as a function of magnetic field at $\nu = 2/3$ and 1.7 K. The vertical dashed lines denote the three energy windows (M1, M2 and M3) for the MCD analysis. **b**, Magnetic-field dependent MCD integrated in window M1, M2 and M3 and normalized to 1 upon saturation at large fields. The solid lines are fits to the Brillouin function. The saturation field B_S obtained from the fit (shown in the key) is insensitive to the choice of the spectral window.

https://doi.org/10.1038/s41565-022-01309-8

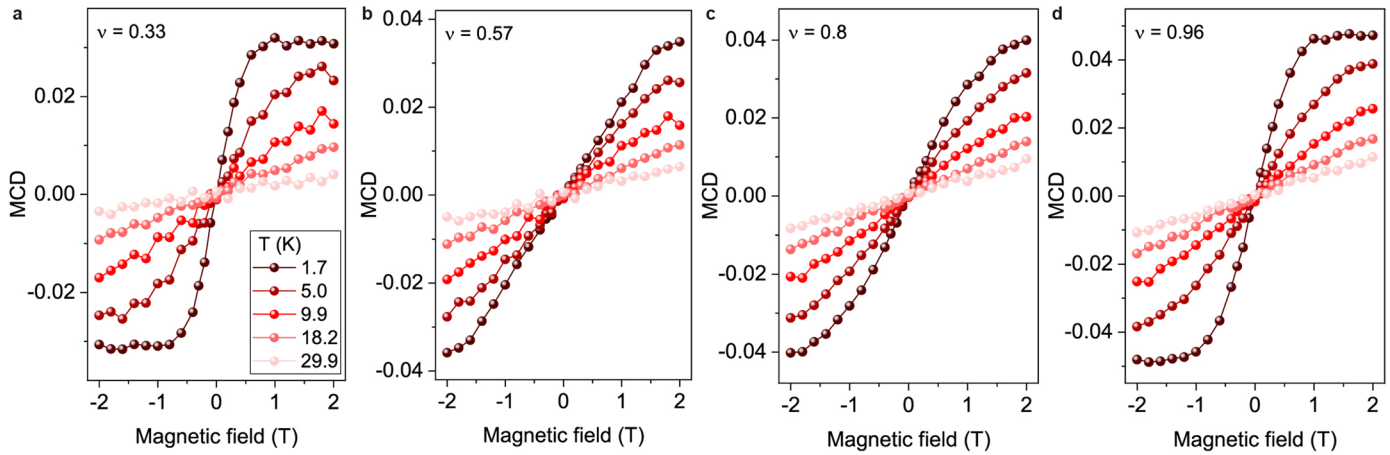

Extended Data Fig. 3 | Magnetic response of device 1 at varying temperatures for $\nu = 0.33$ (a), 0.57 (b), 0.8 (c) and 0.96 (d). The color of the symbols varying from darkest to lightest denotes the temperature from 1.7 to 29.9 K.

https://doi.org/10.1038/s41565-022-01309-8

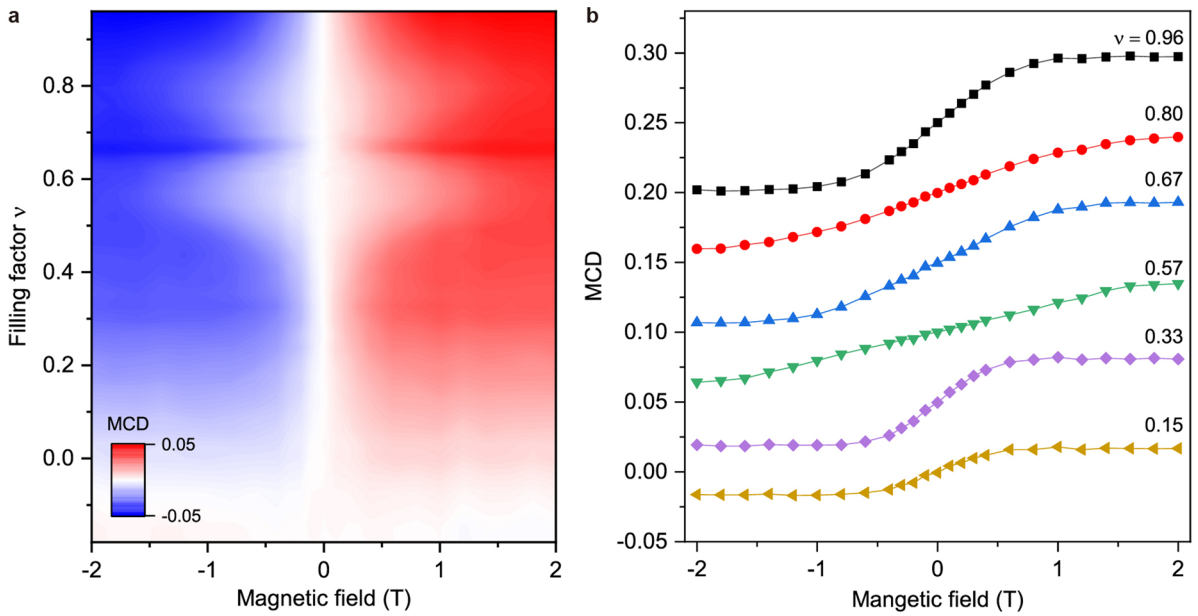

Extended Data Fig. 4 | Magnetic response of device 1 at 1.7 K. a, Integrated MCD as a function of magnetic field and filling factor. **b**, Linecuts of **a** at selected filling factors. The curves are displaced vertically for clarity.

https://doi.org/10.1038/s41565-022-01309-8

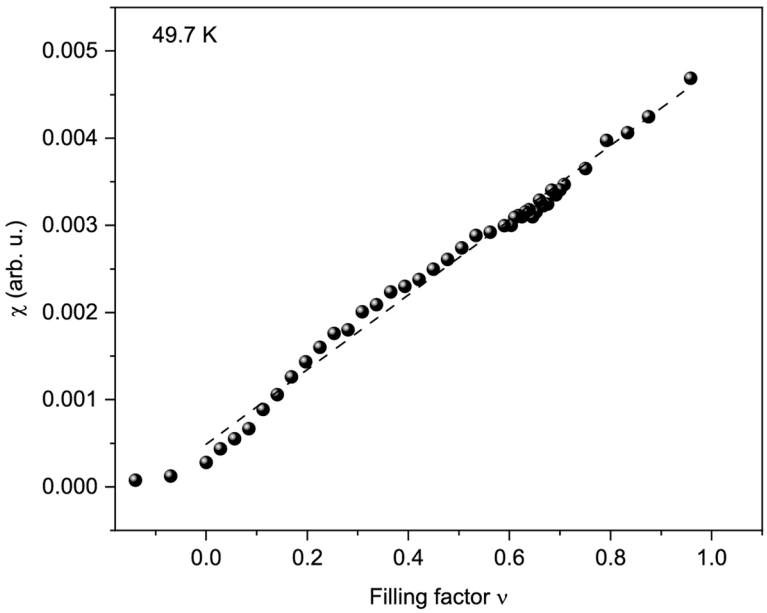

Extended Data Fig. 5 | The magnetic susceptibility as a function of fillings at high temperature (device 1). The dashed straight line is just an eye guidance to the linear filling dependence.

https://doi.org/10.1038/s41565-022-01309-8

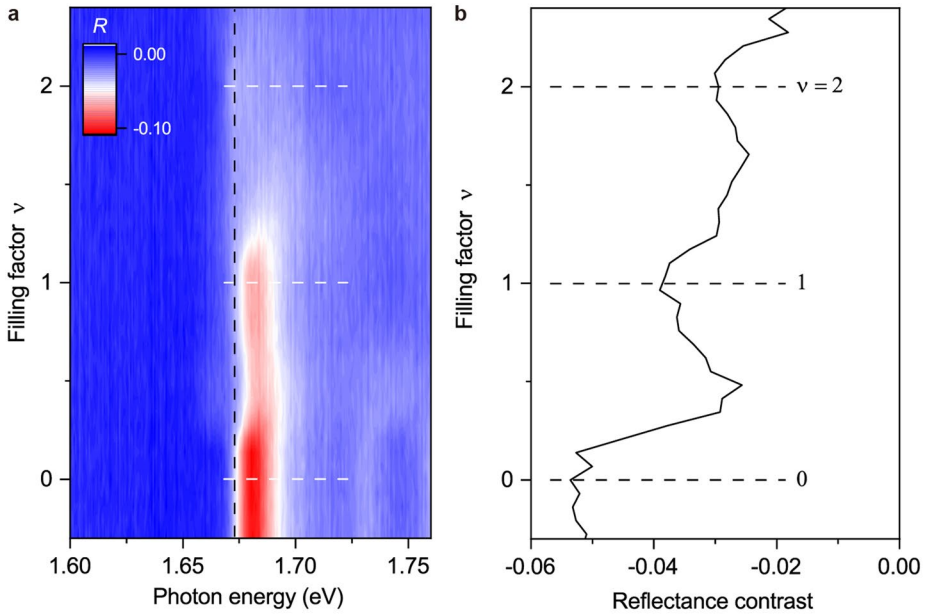

Extended Data Fig. 6 | Optical characterization of device 2 at 1.7 K. a, Filling-dependent reflectance contrast (RC) spectrum. Enhanced RC near the fundamental moiré exciton resonance of WSe_2 is observed only at integer filling factors. The absence of the RC enhancement at $\nu = 1/3$ and 2/3 supports the absence of these Wigner-Mott insulator states. **b**, Linecut of **a** at 1.673 eV.

https://doi.org/10.1038/s41565-022-01309-8

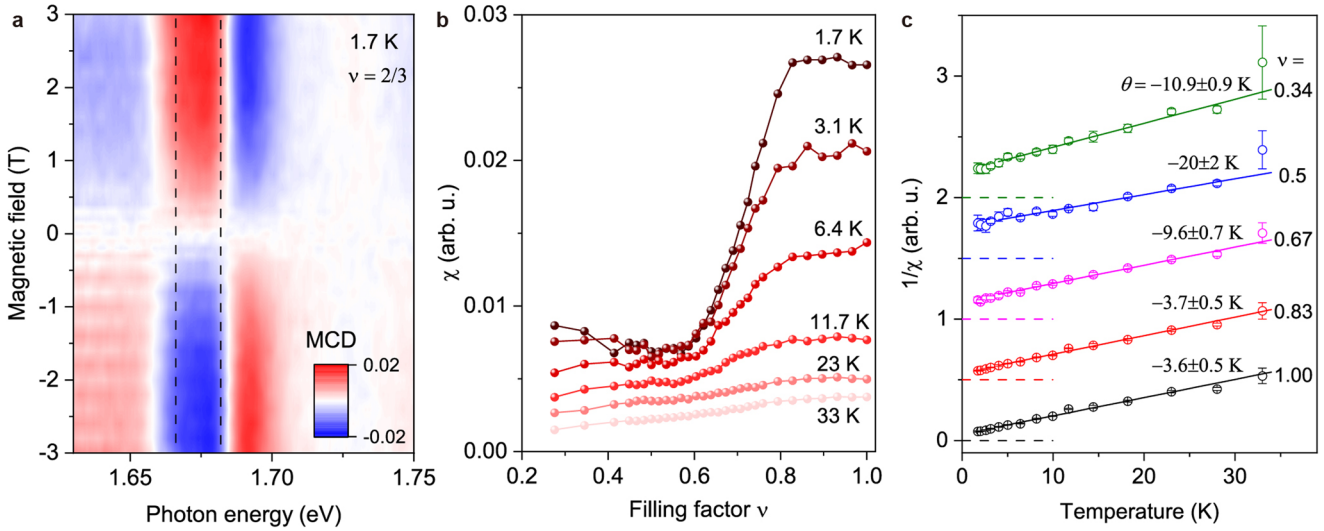

Extended Data Fig. 7 | Magneto-optical measurements (device 2). a, MCD spectrum as a function of magnetic field at $\nu = 2/3$ and T = 1.7 K. The spectrum is integrated over a narrow window around the fundamental moiré exciton resonance (within the two vertical lines) to represent the sample magnetization. **b**, Filling dependence of the magnetic susceptibility, χ, at varying temperatures. The susceptibility is extracted from the linear slope of the magnetic-field dependence of integrated MCD at zero field. The solid lines are guides to the eye. **c**, Curie-Weiss analysis (solid lines) of the inverse susceptibility (symbols) as a function of temperature. The error bars are propagated from the uncertainty of χ. The CW temperatures corresponding to the best fits (solid lines) are included. Data for different filling factors are vertically displaced for clarity. The horizontal dashed lines mark where $1/\chi$ is zero. Linear dependences are observed at temperatures smaller than the CW temperatures; no sign of magnetic ordering is observed (that is no kink in the temperature dependence). The absence of magnetic ordering at temperatures smaller than the mean-field CW temperature signifies the importance of magnetic frustrations in the system.

https://doi.org/10.1038/s41565-022-01309-8

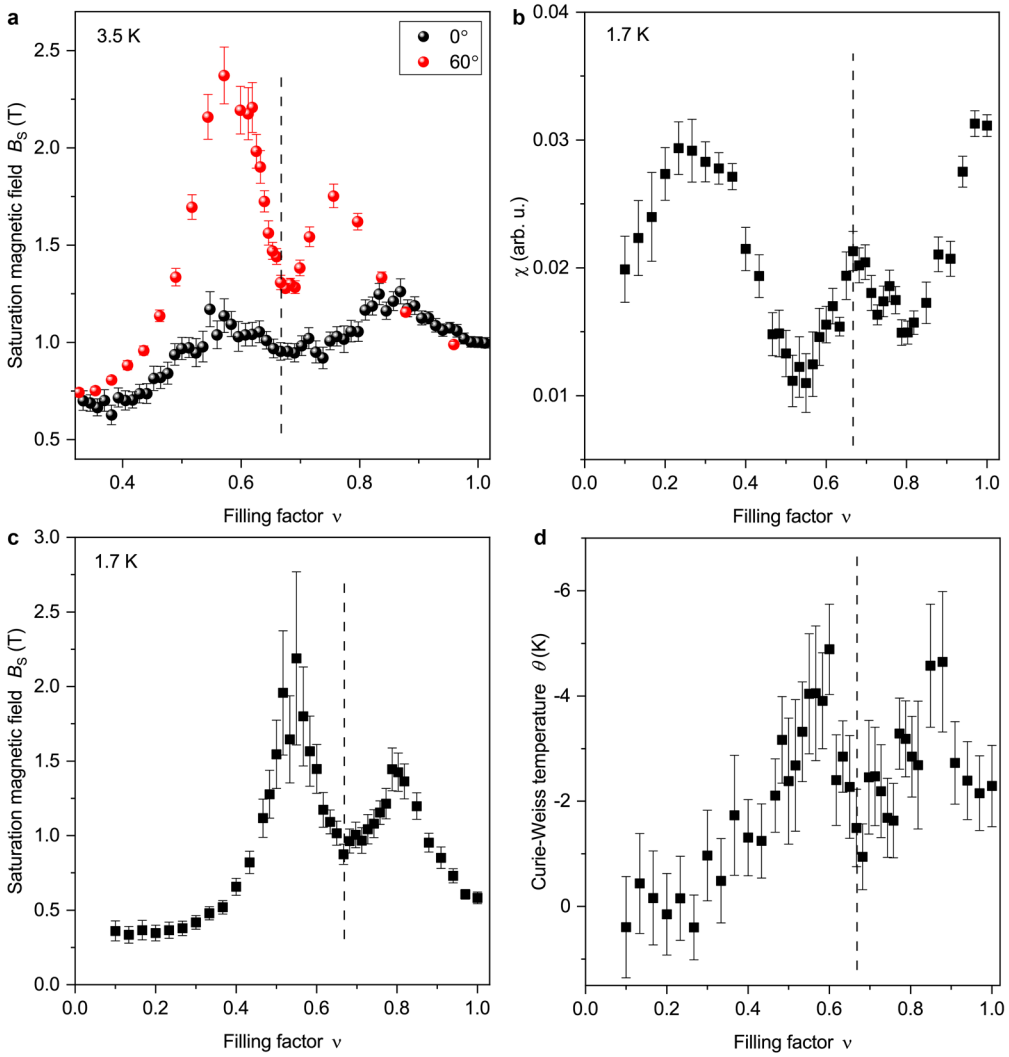

Extended Data Fig. 8 | Results from additional devices. a, Comparison of the filling factor dependent saturation magnetic field of a 0- and 60-degree-aligned sample at 3.5 K. **b**–**d**, Results from another 60-degree-aligned sample, including the filling factor dependence of the magnetic susceptibility at 1.7 K (**b**), the saturation magnetic field at 1.7 K (**c**), and the Curie-Weiss temperature (**d**). The dashed lines denote 2/3 filling, where suppression of AF interactions is observed in all samples. A weaker suppression is observed in the 0-degree-aligned sample, which could be caused by the different moiré structure. The error bars correspond to the uncertainties of the Brillouin-function fit (**a** *and* **c**), the linear *fit to* the field dependence of the MCD *near* zero field (**b**), and the CW analysis (**d**).

https://doi.org/10.1038/s41565-022-01309-8

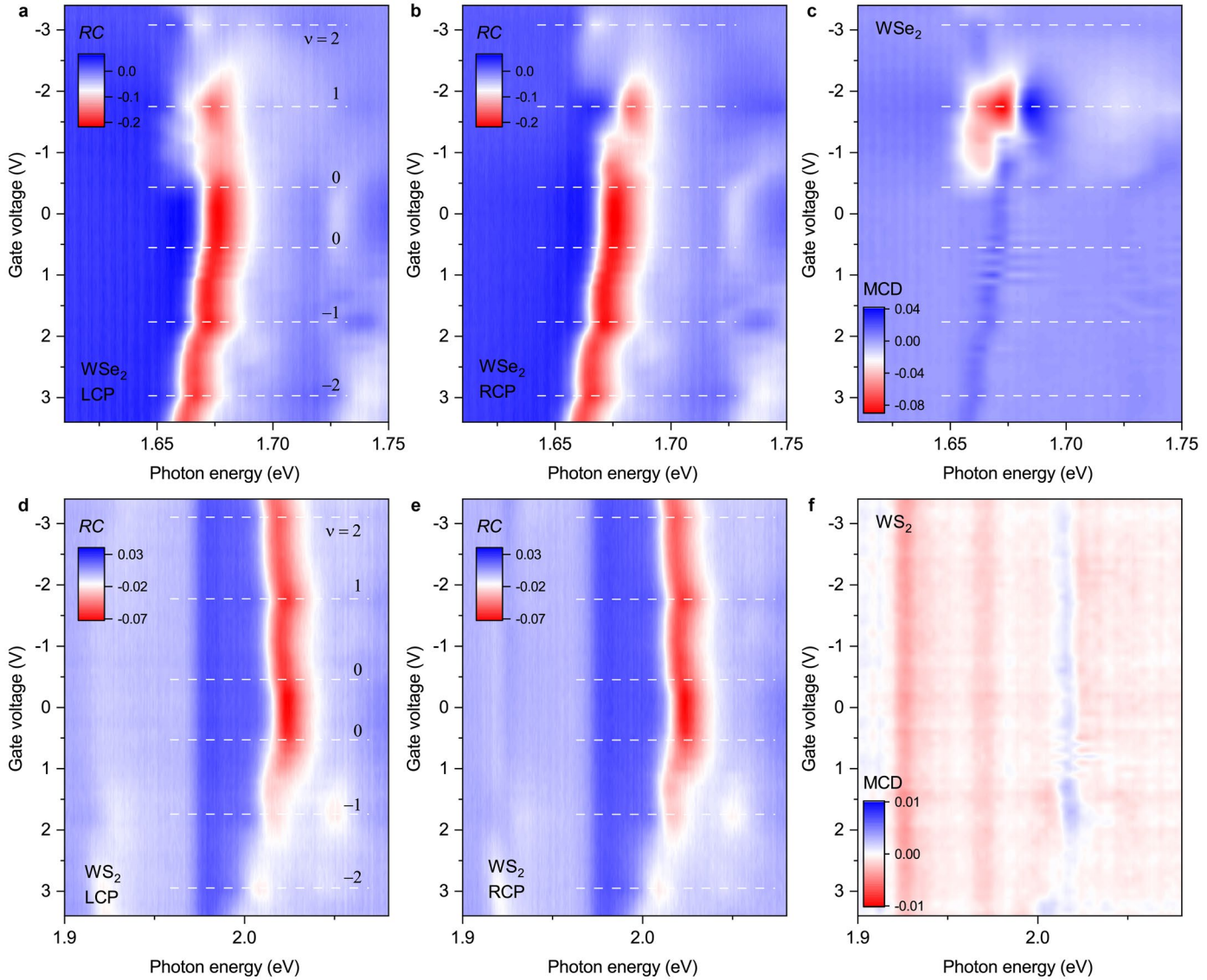

Extended Data Fig. 9 | Helicity-resolved reflectance contrast spectrum as a function of doping for both electron and hole doping. a, b, d, e Gate voltage dependent left- and right-handed reflectance contrast spectrum (LCP and RCP) for the WSe_2 (**a, b**) and WS_2 (**d, e**) layer. The magnetic field is at 2 T. Positive and negative fillings correspond to hole and electron doping, respectively. The dashed lines label the integer filling factors. **c,f**, Extracted gate voltage dependent MCD spectrum for the WSe_2 (**c**) and WS_2 (**f**) layer. Strong MCD response is observed only in the WSe_2 exciton resonance and only for the hole doping case. The results can be understood based on the type-II band alignment in WSe_2/WS_2 bilayers; electron (hole) doping fills the WS_2 (WSe_2) conduction (valence) band. Strong MCD in the WSe_2 layer is expected for hole doping because states near the Fermi level are directly involved in the optical transitions. On the other hand, states near the Fermi level are not involved in the optical transitions for electron doping in W-based TMDs. The MCD response is weak in all cases for electron doping.

https://doi.org/10.1038/s41565-022-01309-8

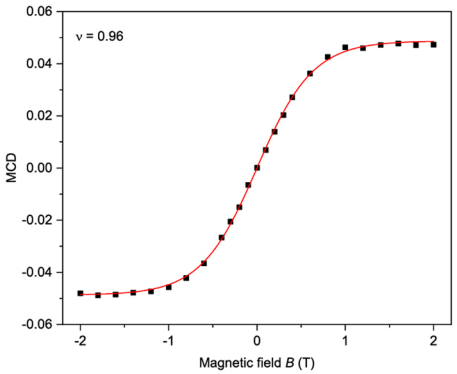

Extended Data Fig. 10 | Determination of the saturation magnetic field (device 1). The red curve is a Brillouin-function fit to the integrated MCD as a function of magnetic field (at 0.96 filling and 1.7 K). The corresponding saturation magnetic field is 0.63 ± 0.01 T.